Performance Limits of Graphene Hot Electron Emission Photoemitters

Ragib Ahsan, Mashnoon Alam Sakib, Hyun Uk Chae, and Rehan Kapadia[*]

*Department of Electrical and Computer Engineering, University of Southern California, Los Angeles,
California, 90089, USA*

Hot electron emission from waveguide-integrated graphene has been recently shown to occur at optical power densities multiple orders of magnitude lower than that of metal tips excited by sub-work-function photons. However, the experimentally observed electron emission currents are small, which limits the practical uses of such a mechanism. Here, we explore the performance limits of hot electron emission in graphene through experimentally calibrated simulations. Two regimes of nonequilibrium emission in graphene are identified, (i) single particle hot electron emission, where an electron is excited by a photon and emitted before losing significant energy through scattering; and (ii) ensemble hot electron emission, where the photon source causes nonequilibrium heating of the electron population beyond the electron lattice temperature. It is shown that, through appropriate selection of photon energy, optical power density, and applied electric field, hot electron emission can be used to create ultrahigh current electron emitters with ultrafast temporal responses in both the single particle and ensemble heating regimes. These results suggest that, through appropriate design, hot electron emitters may overcome the limitations of thermionic and field emitters.

I. INTRODUCTION

From modern electron microscopes to free electron lasers, electron emission devices play an important role in a diverse range of applications [1–6]. Photoemitters constitute a class of electron emitters that uses photons as the source of energy to produce the electron beam. Photoemission occurs via three mechanisms: single-photon emission, multiphoton emission, or strong-field emission. Single-photon emitters, where the incident photon has an energy greater than the work function of the emitter, are the most efficient and broadly used, but also require significant infrastructure, in terms of high-photon-energy lasers or ultrahigh vacuum chambers for negative-electron-affinity emitters. Multiphoton and strong-field emitters allow the use of lower photon energy lasers, potentially enabling the use of compact semiconductor lasers and integrated photonics, but require high power densities ($>10^{15}$ W/m^2), which typically necessitate the use of ultrafast pulsed lasers [7–11]. Recently, it has been shown that hot electrons in graphene can mediate photoemission from sub-work-function photons at power densities over five orders of magnitude lower than that of metal tips [12].

In the previously explored structure, the graphene emitter sits on top of a waveguide that evanescently couples

the photons to the electrons. The thickness (approximately 0.35 nm) of graphene directly addresses the issue of long response time, eliminating the need for the photoexcited electrons to be transported to the emitting surface, as is necessary with standard metallic photoemitters. Favorable scattering rates in graphene also allow the photoexcited hot electrons to be emitted into vacuum before thermalizing down to the Fermi level. Due to these features of graphene, hot electron emission from waveguide-integrated graphene using sub-work-function photons can occur at power densities that are multiple orders of magnitude lower than that of metallic tip emitters [12–15]. Previously, it was shown that an electron emission model obtained by solving the nonequilibrium Monte Carlo Boltzmann transport equation (MCBTE) could quantitatively explain the nature of the observed current density as a function of the applied electric field, optical power density, and photon energy [12,16]. In addition, there have been a number of theoretical studies on graphene-based Schottky barrier devices to model the thermionic and photoexcited electron emission of electrons over the barrier, as well as on generalized two-dimensional material based Schottky barrier devices [17–20]. Here, we theoretically investigate the performance limits of electron emission from graphene within a range of different sub-work-function photon energies, optical power densities, and electric fields, identifying experimental conditions under which high current density, quantum efficiency (η), and ultrafast hot electron photoemitters can operate.

*rkapadia@usc.edu

II. HOT ELECTRON EMISSION MECHANISM IN GRAPHENE

The unique linear band structure of graphene allows its electrons to be excited directly from the valence band to the conduction band within photon energies ranging from far-IR to UV. These photoexcited electrons, referred to as "hot electrons," in graphene are out of equilibrium compared with the initial electron distribution. These nonequilibrium hot electrons, therefore, go through different scattering mechanisms, where they lose energy and thermalize. The most prominent scattering mechanisms in graphene are (1) electron-electron (*e-e*) scattering, (2) optical phonon (OP) scattering, and (3) supercollision acoustic phonon (SC) scattering [12,21–28]. OP scattering includes both longitudinal optical (LO) and transverse optical (TO) phonons. While *e-e* scattering allows the hot electrons to elastically redistribute their excess energy among the "cold" electrons in the Fermi sea, both OP and SC scattering cause them to lose energy to the lattice. When a vertical electric field is applied to graphene, the vacuum barrier bends in response to the field, and these hot electrons can tunnel through the distorted vacuum barrier. In addition to the usual scattering mechanisms, this tunneling mechanism provides another possible pathway for the hot electrons to reach a different final state [12,21]. Probability rates of these mechanisms depend on the energy and momenta of the involved electrons and phonons, as well as the band structure of graphene, and can be quantitatively calculated using Fermi's golden rule. Figure 1 summarizes the basic mechanism of electron emission from graphene.

III. SCATTERING AND TUNNELING RATES

To quantitatively evaluate the electron emission current from graphene as a function of photon energy, optical power density, and electric field, it is important that we quantitatively determine the rates of the scattering
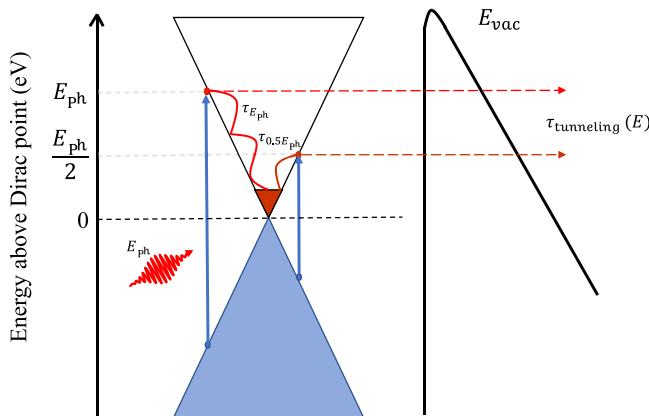
mechanisms and tunneling. Here, Fermi's golden rule is used to calculate the rates [12,29]:

$$\frac{1}{\tau} = \frac{2\pi}{\hbar} \sum_{k,k'} |M(k,k')|^2 [1 - f(k')]\delta_E. \quad (1)$$

Here, $1/\tau$ is the scattering rate, $M(k,k')$ is the matrix element for the transition between the initial state $|k\rangle$ to the final state $|k'\rangle$, $f(k)$ is the Fermi-Dirac distribution, and δ_E ensures the energy conservation. For different scattering mechanisms, the matrix element will be different, and therefore, lead to different scattering rates. Calculations of each of the scattering rates are carried out following previous work [12].

Figure 2(a) shows the scattering rates for all scattering mechanisms as a function of electron energy for an electronic temperature of 300 K, while Fig. 2(b) summarizes the total scattering rates for different electronic temperatures. Since increasing the electronic temperature increases the number of electrons in the Fermi sea, the *e-e* scattering increases significantly. This ultimately leads to an increase in the overall scattering rates with increasing electronic temperature. The tunneling rates for different electric fields are shown in Fig. 2(c). Electrons with higher energy see a smaller barrier, and therefore, have larger tunneling rates. On the other hand, when the electric field is increased, the nearly triangular vacuum barrier is further thinned, and there is an exponential increase in the tunneling rate. Therefore, an electron with higher energy will be able to tunnel the barrier more frequently, if a larger electric field is applied.

IV. RESULTS FROM THE MCBTE SOLVER

The MCBTE simulation uses the calculated scattering rates to determine the energy-time trajectory of the hot electrons. An open-source Monte Carlo simulator, Archimedes, is modified to solve the MCBTE for graphene [16]. The MCBTE solving approach is discussed in more detail in the Supplemental Material [30]. The simulation is initialized with 5×10^6 electrons, which is equivalent to simulating 0.5 μm^2 graphene. Figure 2(d) shows the calculated trajectories for four different photon energies, when the electronic temperature is 300 K. The trajectories are obtained by tracking the average energy of 50 photoexcited electrons during each simulation and then averaging over 50 different simulations. The trajectory for 1 eV photons shows us three distinct regions: (1) an initial drop in electron energy due to *e-e* scattering, (2) dissipation of energy due to OP scattering until the electron energy goes below the OP energy (approximately 190 meV), and (3) a slower dissipation in energy due to SC scattering. Since *e-e* scattering rates are considerably smaller than the OP scattering rates for higher energy electrons, the *e-e* scattering dominated initial energy loss cannot be observed

FIG. 1. Emission of photogenerated hot electrons from graphene, while they go through the scattering processes.
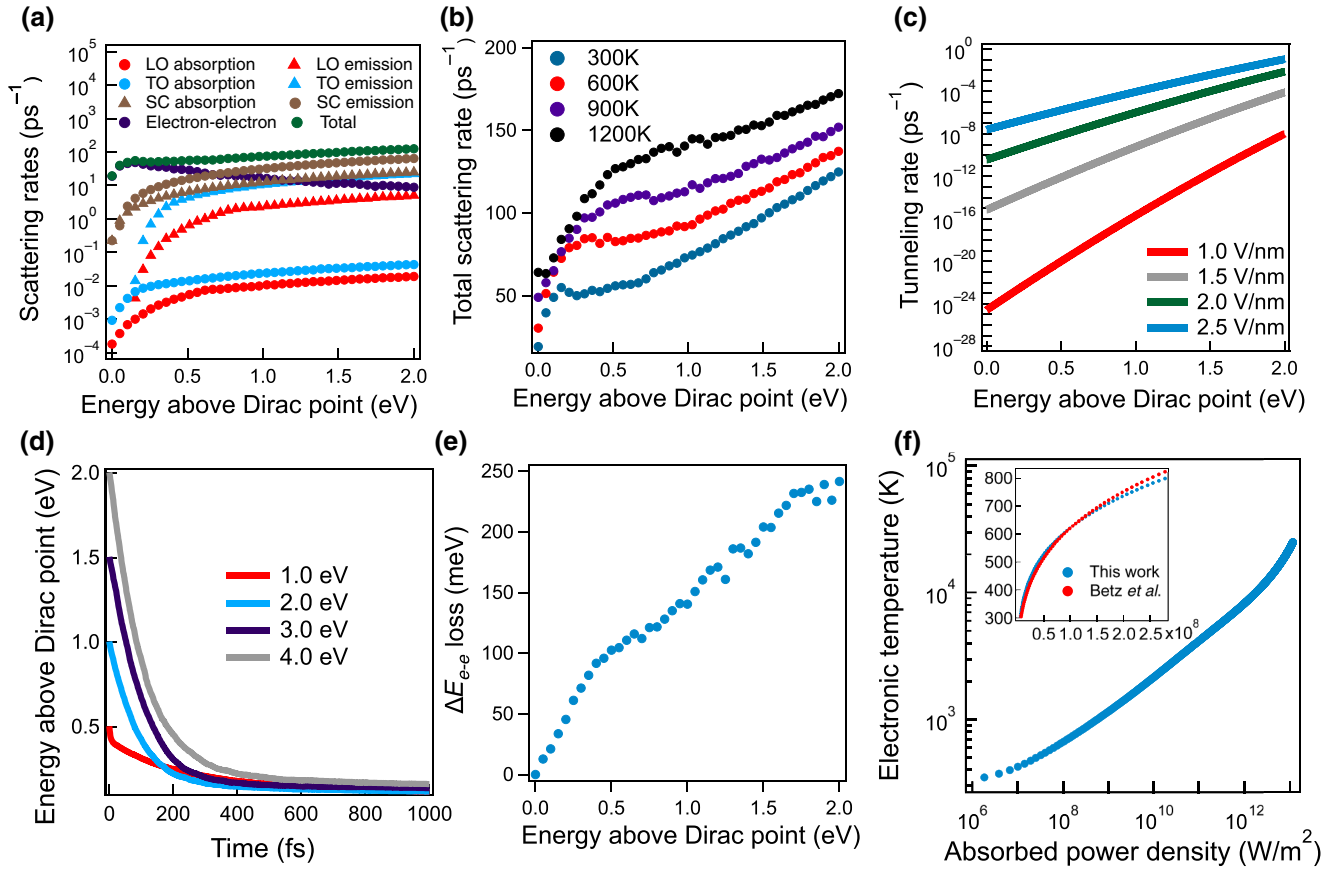
FIG. 2.   Simulation of hot electron scattering, electron emission, and electronic temperature. (a) Hot electron scattering rates for the major scattering mechanisms of graphene for electronic temperature of 300 K. (b) Total scattering rates for different electronic temperatures. (c) Energy-resolved tunneling rates for hot electrons in graphene. (d) Simulated time-resolved energy trajectory of hot electrons excited by different photon energies. (e) Average energy lost by hot electrons due to *e-e* scattering. (f) Simulated electronic temperature of graphene as a function of absorbed optical power density. The inset shows the electronic temperature for smaller absorbed optical power densities in linear scale.

in the trajectories obtained for higher energy photons. Average energy loss of hot electrons due to *e-e* scattering events is shown in Fig. 2(e). Figure 2(f) shows the change in electronic temperature as a function of absorbed optical power density. Using these scattering rates, the calculated electronic temperature profile is shown to match the temperature experimentally observed by Betz *et al.* [12,23].

A. Emission current model

We model the emission current using a quantum mechanical tunneling model [12,31–34]. Throughout the paper, when we mention thermalized electrons, we refer to the electrons that follow the Fermi-Dirac distribution with a well-defined electronic temperature. This temperature may be that of the lattice or, under specific excitation conditions, may be higher than the lattice temperature itself. When these electrons are emitted from the material over the vacuum barrier without any influence from the electric field, we define the current density due to this flux as the

"thermionic emission" current density. However, under the influence of the electric field, there will be an increased flux of emitted electrons, as they have a finite rate of tunneling through the barrier. We define this enhanced emission current density as the "thermionic field emission" (TFE) current density, which can be expressed as

$$J_{\text{TFE}}(T,F) = e \int_{-\infty}^{\infty} D(E) r_T(E,F) f(E,T) dE. \qquad (2)$$

Here, T is the electronic temperature, E is the energy of the electron, F is the electric field, e is the elementary charge, $D(E)$ is the density of states of graphene [35], $r_T(E,F)$ is the tunneling rate, and $f(E,T)$ is the Fermi-Dirac distribution. This model for TFE current density was developed by Sinha *et al.* [36] and Ang *et al.* [17], while Rezaeifar *et al.* redeveloped it with numerical implementation [12]. For different optical power densities, we find the electronic temperature from Fig. 2(f) and evaluate the integral numerically to calculate the current density due to thermal electrons.

To calculate the emission current due to photoexcited electrons, we consider the possibility of multiphoton absorption (MPA) [37,38], so that every absorbed photon results in n photoexcited electron-hole pairs for n-photon absorption, and therefore, we calculate the generation rate from the relation $S = \sum_{i=1}^{n} G_i(S, E_{ph})E_{ph} \times i$. Here, S is the absorbed power density and $G_i = (\tau_1/\tau_i)G_1$ is the generation rate for the i-photon absorption process. We explain the details of the calculation of the i-photon absorption rate, τ_i, in the Supplemental Material [30]. Figure 3(a) shows the ratio of the two-photon absorption (TPA) rate to the single-photon absorption (SPA) rate for different photon energies and power densities. Now, we can calculate the emission current due to hot electrons (HEs) from the following relation [12]:

$$J_{HE}(S, F) = \sum_{i=1}^{n} \int_{0}^{\infty} eG_i(S, E_{ph})r_T[E(t), F]dt. \quad (3)$$

Here, $E(t)$ is the energy of the hot electron as a function of time, as shown in Fig. 2(d), where $E(0) = (nE_{ph}/2)$ for the n-photon absorption.

V. CALCULATION AND ANALYSIS OF THE EMISSION CURRENT DENSITY

Using these relationships, we calculate the current densities for four different photon energies (1–4 eV) for a power density of 10^4 W/m^2 as we vary the electric field from 0.5 to 5 V/nm. The reason behind choosing 10^4 W/m^2 is to investigate the current density when there is no significant heating of the electron population. We ignore electronic temperature deviation below a power density of about 10^6 W/m^2, as the electronic temperature does not deviate significantly. We consider MPA processes to order:, $n = 3$ for $E_{ph} = 1$ and 2 eV and $n = 2$ for $E_{ph} = 3$ and 4 eV. Figure 3(b) shows the calculated hot electron current densities for different photon energies and the TFE current density. At smaller electric fields, the thermal electrons see a wider and larger energy barrier for tunneling, whereas the high-energy electrons see a narrower and smaller energy barrier. Therefore, the hot electron component dominates at smaller electric fields over the thermal component, as observed for the case of higher energy photons (>1 eV). At even smaller electric fields, the MPA processes dominate over SPA for higher photon energies. There are two competing factors that determine whether
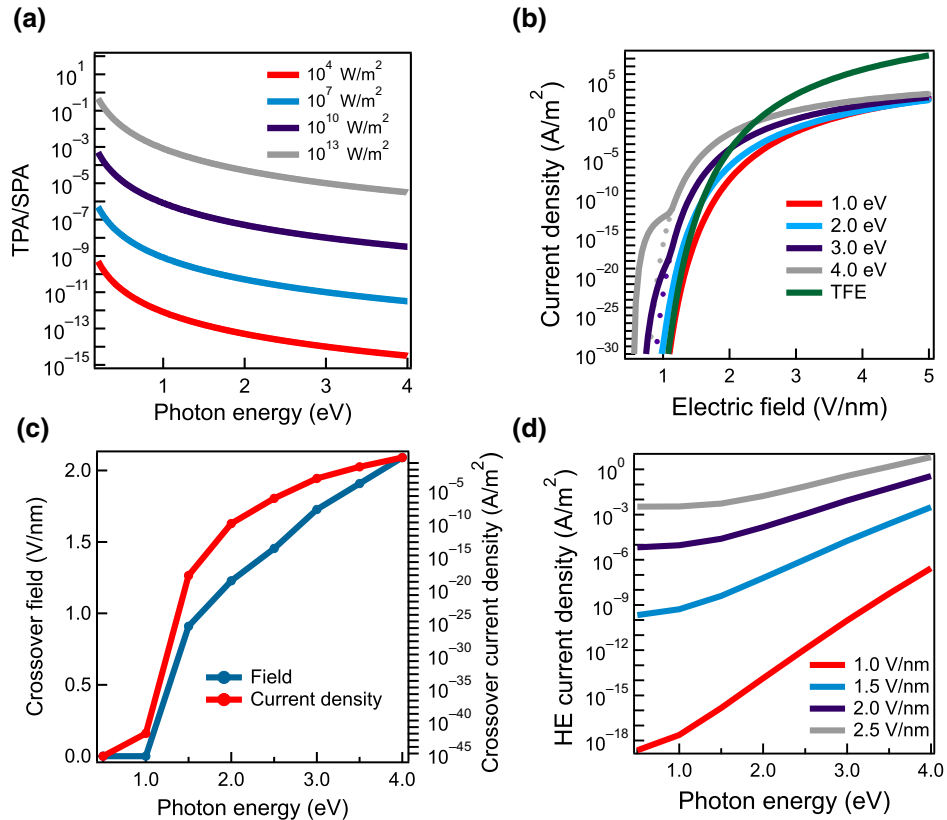
FIG. 3. Electron emission current calculation for low power density photoexcitation. (a) Ratio of TPA rate to SPA rate in graphene at different absorbed power densities. (b) Simulated HE and TFE current density for different photon energies at an absorbed power density of 10^4 W/m^2 (dots: SPA, connected lines: MPA). (c) Crossover electric field and current densities as a function of photon energy. (d) HE current density as a function of photon energy for different electric fields.
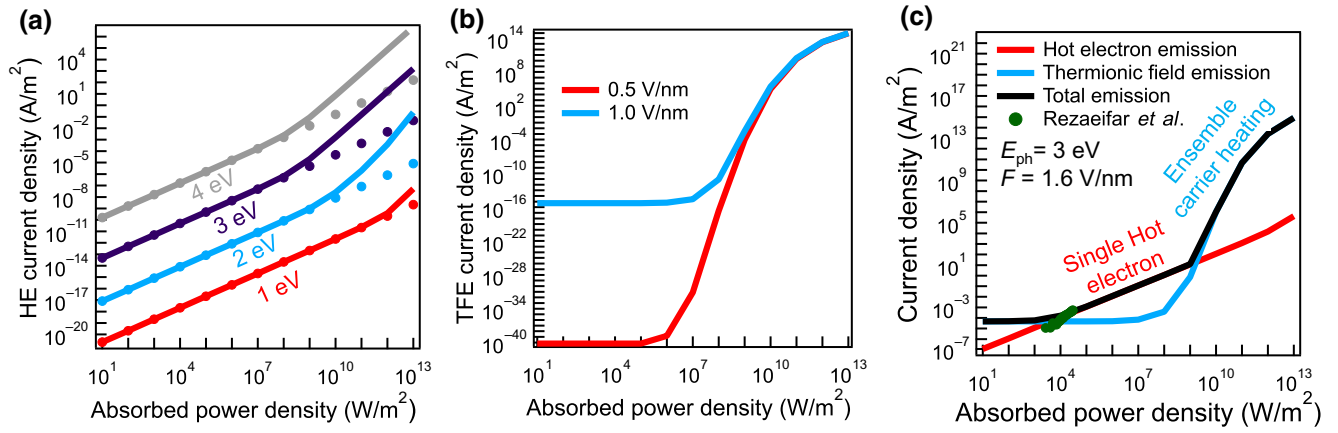
FIG. 4. Electron emission current calculation for large power densities. (a) Calculated HE current density for different photon energies at an electric field of 1.0 V/nm (dots, SPA; connected lines, MPA). (b) Calculated TFE current density at 0.5 and 1.0 V/nm fields. (c) Crossover between different emission mechanisms at different ranges of absorbed power densities calculated at 1.6 V/nm for photoexcitation by 3 eV photons.

SPA or MPA process will dominate the observed current density: (1) energy of the hot electron and (2) efficiency of the MPA process. The initial energy difference between an electron that absorbs one photon and an electron that absorbs n photons is the energy of $(n-1)$ photons. The tunneling rate increases exponentially with an increase in electron energy [12]. However, the magnitude of current density due to MPA under these conditions is below the threshold current density likely to be observed in an experiment. From Fig. 3(b), we can observe a clear crossover between the hot electron dominated regime and the TFE-dominated regime. However, for 1 eV photons and below, the hot electron current is not significant enough within the electric field range considered and no crossover can be observed. Figure 3(c) shows the crossover fields and current densities as a function of photon energy. For higher photon energies, the crossover field increases at a nearly linear rate, and therefore, the crossover current densities increase by several orders of magnitude. Figure 3(d) shows the hot electron current density as a function of photon energy for different electric fields. We can see an exponential increase in current density with increasing photon energies. However, the increase is less steep for larger electric fields, as the barrier gets thinner, and the difference in barrier heights plays a less effective role in determining the tunneling rates. For lower photon energies, the difference in barrier heights is even smaller and the increase in HE current is even less prominent. The most significant observation from these calculations is that there is a distinct crossover field for every photon energy below which hot electrons will dominate the emission current, and for the same power density of different photon energies and the same electric field below the crossover field, the efficiency of converting photons into emitted electrons will be higher for higher photon energies.

For power densities of $>10^6$ W/m^2, the electron population will heat up to a temperature that is significantly greater than that of the lattice temperature (300 K). In addition to cold-field emission and single hot electron emission, this electronic heating leads to the emission of ensemble hot electrons [39,40]. Figure 4(a) shows the calculated HE current densities for an electric field of 1 V/nm, considering the different hot electron trajectories obtained for the electronic temperatures produced by the corresponding power densities. MPA processes exceed the SPA process only at higher power densities. The corresponding TFE current densities due to ensemble carrier heating are shown in Fig. 4(b). For power densities of $>10^9$ W/m^2, the electronic temperature rises above 1000 K and the effect of increasing electric field becomes insignificant. Figure 4(c) shows the different components of the total emission current density for $E_{ph} = 3$ eV and $F = 1.6$ V/nm. Here, we can identify three different mechanisms of electron emission that dominate at different ranges of power densities: (1) field emission at small power densities, (2) single hot electron emission at intermediate power densities, and (3) ensemble hot electron emission at large power densities. Since both the hot electron generation rate and electronic heating are small at smaller power densities, this regime is dominated by the tunneling of thermal electrons within a few $k_B T$ ($\sim$26 meV) of the Fermi level, i.e., cold-field emission. For intermediate power densities, electronic heating is still insignificant, whereas the generation rates increase proportionally, and hence, this regime is dominated by the single hot electron emission. Beyond this regime, electronic heating becomes more significant and thermionic emission due to ensemble hot electrons dominates. Figure 4(c) also shows the experimentally measured electron emission current reported by Rezaeifar *et al.* for the same electric field and photon
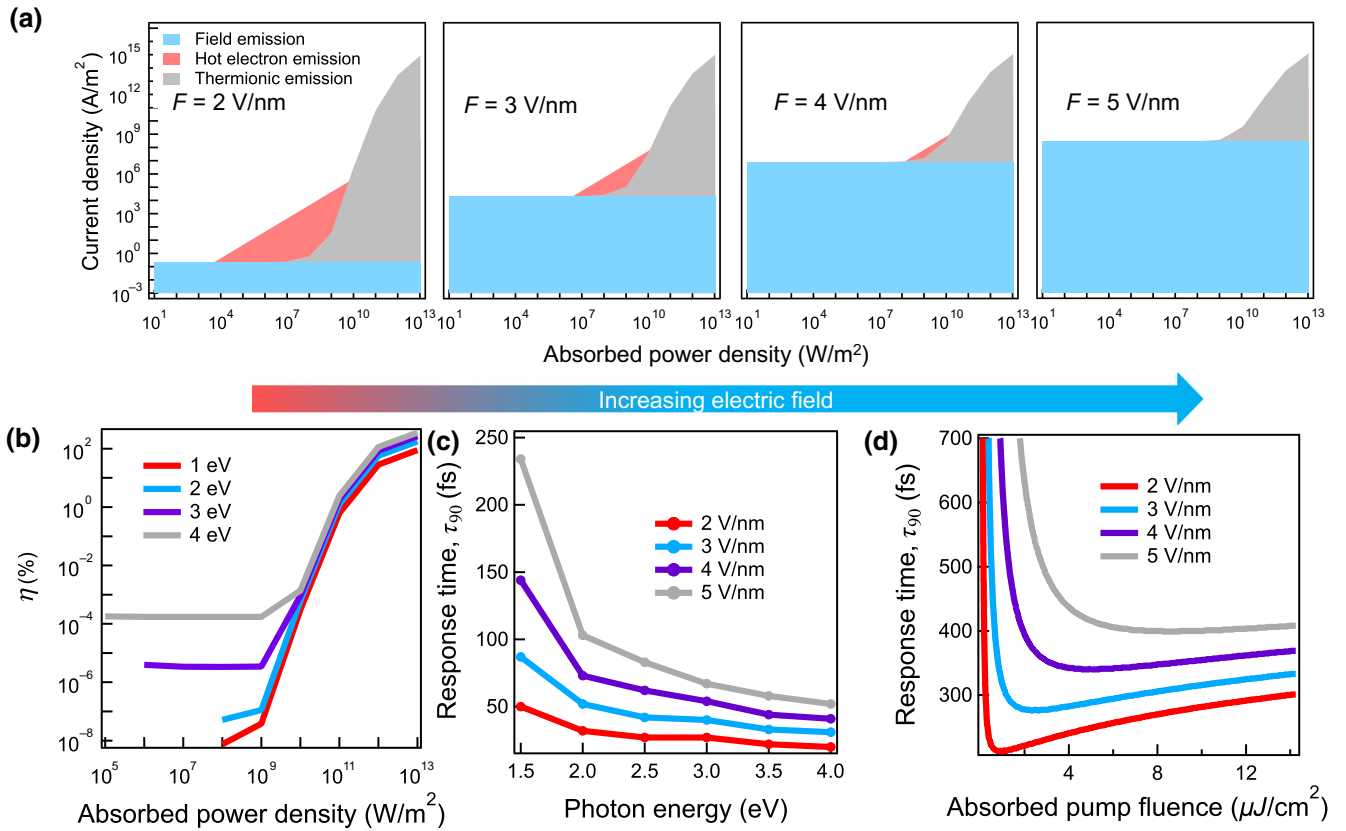
FIG. 5.   Performance limits of the photoemitter. (a) Change in the electron emission mechanism with increasing electric field for $E_{ph} = 4$ eV. (b) η for different photon energies and power densities. Response time of the photoemitter in the (c) HE and (d) electronic heating regimes.

energy, which shows good agreement with our theoretical values [12].

Figure 5(a) shows the individual emission components for $E_{ph} = 4$ eV and different electric fields from 2 to 5 V/nm, to further elucidate how the electron emission mechanism changes between these three regimes. The number of thermal electrons is very large relative to the number of hot electrons before electronic heating begins. As a result, the increase in electric field favors field emission. This effect can very easily be seen in Fig. 5(a), as the HE regime is completely overcome by the field-emission regime at 5 V/nm. For the thermionic emission regime, the increasing electric field does not change the emission current significantly, as observed in Fig. 4(b).

VI. EXPERIMENTAL ROAD MAP TO PERFORMANCE LIMITS

Using the established tools, η, response time, and current density are interrogated. Figure 5(b) shows the η of the graphene photoemitter as a function of absorbed power density for multiple photon energies and an electric field of 2 V/nm. Photoemission η is not a defined quantity in the field-emission-dominated regime, and therefore, we show

η only for the single and ensemble hot electron emission regimes. In the single hot electron regime, current density increases linearly with absorbed power density, and hence, η becomes constant over this range. Photon energy determines the crossover power density between field emission and hot electron regimes. While hot electron emission starts dominating at a power density of 10^2 W/m^2 for 4 eV photons, with a η of about 10^{-6}, 1 eV photons require a power density of 10^7 W/m^2 before moving on to the hot electron regime with a significantly smaller η of about 10^{-11}. For increasing electric fields, this constant η in the HE regime increases and can exceed 100% for electric fields higher than about 4.8 V/nm for $E_{ph} = 4$ eV, as shown in Fig. S3 within the Supplemental Material [30]. For single photon photoemission or single photon hot electron emission, it is not possible to get a η exceeding 100%. However, when there is ensemble carrier heating, the redistribution of excess energy between the photoexcited hot electrons and the cold electrons via e-e scattering causes the sea of cold electrons to become hot as well. As a result, the energy of a single photon can potentially be transferred to many electrons, leading to a seemingly counterintuitive photoemission η that exceeds 100%. However, it should be noted that the power conversion efficiency will still be

dramatically lower than 100%. In this ensemble carrier heating regime, the true potential of graphene photoemitter is unleashed as the η of the device goes above 100% at absorbed power densities above 10^{11} W/m^2, irrespective of the applied electric field. For typical bulk and even thin-film metallic photoemitters, the experimentally observed η is always well below 100% [39,41–47]. While theoretically it may be possible to achieve such a high η for metallic photoemitters, the required power density to raise the electronic temperature would be orders of magnitude higher than that of graphene, primarily because achieving electronic heating in bulk metals requires large amounts of energy deposited very quickly, and the resulting carriers quickly scatter down, which reduces the electronic temperature below the critical temperature that would allow a $\eta > 100\%$.

For pulsed photoexcitation, it is important for a photoemitter to provide an ultrafast response. Response time (τ_{90}) is defined as the time required for the photoemission current to drop down to 10% of its initial value [7,48]. However, this response time depends on the regime the photoemitter is working on. For low-energy pulses, there is no electronic heating, and therefore, the HE process dominates the emission current. As a result, the response time is determined by how fast the energy of the photoexcited hot electron decays, as well as the energy-resolved tunneling rate of the electrons. In Fig. 5(c), we use the energy trajectories [Fig. 2(d)] obtained from the MCBTE solver and the energy-resolved tunneling rates [Fig. 2(c)] to calculate τ_{90} for the HE-dominated regime for the graphene photoemitter. Higher photon energies result in larger tunneling rates, and therefore, provide shorter response times. Larger electric fields increase the tunneling rate for all energies, and therefore, the decay in emission current slows down, resulting in an increase in the response time. The negligible thickness of graphene ensures that the hot electrons are always at the emitting surface, thereby eliminating the transport time to the surface. This essentially enables graphene to respond to the absorbed photons on the sub-picosecond timescale, going as short as about 20 fs. However, for high-energy pulses, there is significant electronic heating, which makes thermionic emission the dominant emission mechanism. Using the energy-dependent scattering rates obtained from the MCBTE solver, we can calculate the temporal evolution of the electronic temperature for a given absorbed pump fluence, i.e., energy density. From this electronic temperature profile, we calculate the time-resolved current densities, and therefore, the response time. Figure 5(d) shows the graphene photoemitter response times for the thermionic emission dominated regime for different absorbed pump fluences. It is noteworthy to mention that photon energy does not play a significant role in determining the response time in this regime, since the emission current is predominantly coming from the thermalized hot electrons. We can observe

two different regimes for the response time: (1) a drastic decrease in response time, as the absorbed energy density increases in the lower energy density regime; and (2) a slower increase in response time, as the absorbed energy density increases in the higher energy density regime. There are two competing mechanisms that cause this. First, there is an electronic temperature-dependent cooling rate and, second, when the energy dependence of tunneling rates increases, the time dependence of current emission decreases. At low energy densities, the electronic temperature rises quickly with increasing energy density due to the small density of states available in graphene at lower energies [Fig. S4(b) within the Supplemental Material [30]]. Thus, the key mechanism leading to the initial decrease in response time is the rapid increase in temperature leading to both increased cooling rates and larger changes in current for the same temperature drop, due to the superlinear current-temperature relationship. For higher energy densities, the increase in electronic temperature is significantly reduced, as shown in Fig. S4(b) within the Supplemental Material [30], due to the larger graphene density of states [30]. However, at further increased energy densities, thermionic emission becomes the dominant mechanism, which has a reduced temperature dependence compared with that of the thermionic field emission. Thus, the response times increase. As observed for the HE regime response times, a higher electric field results in longer response times for the thermionic emission dominated regime as well. In this regime, we observe a subpicosecond response time within the range of 250 to 500 fs. Therefore, there is a trade-off between maximum current and response time, which forces us to choose whether to operate the photoemitter in the lower current and faster response HE regime or the higher current and slower response thermionic emission regime. Nevertheless, this opens the way to realizing ultrafast subpicosecond photoemitters with extremely high current for commercial applications. Integrating optical cavities, such as ring resonators and Fabry-Perot resonators, with the graphene photoemitter, as well as engineering the field enhancement factor using nanoscale tips, we can achieve high power densities and electric fields to design arrays of commercially viable photoemitters [49,50]. Although this work exclusively focuses on monolayer graphene photoemitters, it is also possible to qualitatively comment on the performance of few-layer graphene photoemitters from this study. While an n-layer graphene ($n > 1$) potentially offers a greater higher optical absorption and carrier density due to the extra layers, any photoexcited hot electron in the i-th layer from the bottom would be required to transport to the top emitting surface layer ($i = n$). During this transport, we would expect this hot electron to have $n-i$ times the probability of getting scattered by optical phonons and subsequently losing about $(n-i)\,E_{\mathrm{OP}}$ energy, where $E_{\mathrm{OP}} \approx 200$ meV is the optical phonon energy in graphene. Due to this additional loss

in energy, the tunneling rate, and consequently, the emission current, will decrease. We believe that the monolayer nature of graphene, which allows the hot electrons to be at the emitting surface at all times, plays a very significant role in exhibiting the exceptionally good photoemission properties predicted by our study.

VII. CONCLUSION

We investigate the performance limits of a graphene photoemitter using a MCBTE solving approach. Our theoretical calculations show that there are two key hot electron emission mechanisms: single and ensemble hot electron emission. These two mechanisms can be easily identified due to the existence of a critical optical power density ($\sim 10^9$ W/m^2) that clearly distinguishes the emission current between two different regimes. Below the critical optical power density, emission current is dominated by the emission of single hot electrons, while, above this critical power density, significant electronic heating beyond the lattice temperature triggers the ensemble hot electron emission. In the ensemble hot electron emission regime, it is possible to obtain a photoemission $\eta > 100\%$, as well as an emission current density exceeding 100 mA/μm^2. These graphene photoemitters can be operated with ultrafast sub-picosecond response times, while maintaining an ultrahigh emission current. We further verify the accuracy of our predictions, showing good quantitative agreement between experimentally measured and theoretically calculated current densities. This prediction provides an experimental road map towards realizing the performance limits of graphene photoemitters and building next-generation electron emission sources that can address the limitations of present-day photoemitters.

ACKNOWLEDGMENTS

[1] D. Misell and C. Stolinski, Scanning electron microscopy and X-ray microanalysis. A text for biologists, material scientists and geologists JI Goldstein, DE Newbury, P. Echlin, DC Joy, C. Fiori and E. Lifshin. Plenum Press, New York and London, 1981. XIII+ 673 pp.£ 29.50, Pergamon (1983).

[2] C. Vieu, F. Carcenac, A. Pepin, Y. Chen, M. Mejias, A. Lebib, L. Manin-Ferlazzo, L. Couraud, and H. Launois, Electron beam lithography: Resolution limits and applications, Appl. Surf. Sci. **164**, 111 (2000).

[3] C. Brau, *Free-electron Lasers* (Academic Press, Boston, MA, USA, 1990) xi.

[4] L. Reimer, *Transmission Electron Microscopy: Physics of Image Formation and Microanalysis* (Springer-Verlag, New York, 2013).

[5] D. M. Goebel and I. Katz, *Fundamentals of Electric Propulsion: ion and Hall Thrusters* (John Wiley & Sons, 2008).

[6] J. Benford, J. A. Swegle, and E. Schamiloglu, *High Power Microwaves* (CRC press, Boca Raton, Florida, USA, 2015).

[7] I. V. Bazarov, B. M. Dunham, Y. Li, X. Liu, D. G. Ouzounov, C. K. Sinclair, F. Hannon, and T. Miyajima, Thermal emittance and response time measurements of negative electron affinity photocathodes, J. Appl. Phys. **103**, 054901 (2008).

[8] I. V. Bazarov, B. M. Dunham, and C. K. Sinclair, Maximum Achievable Beam Brightness From Photoinjectors, Phys. Rev. Lett. **102**, 104801 (2009).

[9] B. Dunham, J. Barley, A. Bartnik, I. Bazarov, L. Cultrera, J. Dobbins, G. Hoffstaetter, B. Johnson, R. Kaplan, and S. Karkare, Record high-average current from a high-brightness photoinjector, Appl. Phys. Lett. **102**, 034105 (2013).

[10] C. Gulliford, A. Bartnik, I. Bazarov, L. Cultrera, J. Dobbins, B. Dunham, F. Gonzalez, S. Karkare, H. Lee, and H. Li, Demonstration of low emittance in the Cornell energy recovery linac injector prototype, Phys. Rev. Spec. Top.-Accel. Beams **16**, 073401 (2013).

[11] S. Karkare, L. Boulet, L. Cultrera, B. Dunham, X. Liu, W. Schaff, and I. Bazarov, Ultrabright and Ultrafast III–V Semiconductor Photocathodes, Phys. Rev. Lett. **112**, 097601 (2014).

[12] F. Rezaeifar, R. Ahsan, Q. Lin, H. U. Chae, and R. Kapadia, Hot-electron emission processes in waveguide-integrated graphene, Nat. Photonics **13**, 843 (2019).

[13] R. Bormann, M. Gulde, A. Weismann, S. Yalunin, and C. Ropers, Tip-Enhanced Strong-Field Photoemission, Phys. Rev. Lett. **105**, 147601 (2010).

[14] W. P. Putnam, R. G. Hobbs, P. D. Keathley, K. K. Berggren, and F. X. Kärtner, Optical-field-controlled photoemission from plasmonic nanoparticles, Nat. Phys. **13**, 335 (2017).

[15] B. Barwick, C. Corder, J. Strohaber, N. Chandler-Smith, C. Uiterwaal, and H. Batelaan, Laser-induced ultrafast electron emission from a field emission tip, New J. Phys. **9**, 142 (2007).

[16] J. M. Sellier, J. E. Fonseca, and G. Klimeck, in *2012 15th International Workshop on Computational Electronics, IEEE* (2012), pp. 1–4.

[17] Y. S. Ang, H. Y. Yang, and L. Ang, Universal Scaling Laws in Schottky Heterostructures Based on Two-dimensional Materials, Phys. Rev. Lett. **121**, 056802 (2018).

[18] Y. S. Ang, Y. Chen, C. Tan, and L. Ang, Generalized High-Energy Thermionic Electron Injection at Graphene Interface, Phys. Rev. Appl. **12**, 014057 (2019).

[19] M. Trushin, Theory of thermionic emission from a two-dimensional conductor and its application to a graphene-semiconductor Schottky junction, Appl. Phys. Lett. **112**, 171109 (2018).

[20] M. Trushin, Theory of photoexcited and thermionic emission across a two-dimensional graphene-semiconductor Schottky junction, Phys. Rev. B **97**, 195447 (2018).

[21] Q. Ma, T. I. Andersen, N. L. Nair, N. M. Gabor, M. Massicotte, C. H. Lui, A. F. Young, W. Fang, K. Watanabe,

and T. Taniguchi, Tuning ultrafast electron thermalization pathways in a van der Waals heterostructure, Nat. Phys. **12,** 455 (2016).

[22] M. Breusing, S. Kuehn, T. Winzer, E. Malić, F. Milde, N. Severin, J. Rabe, C. Ropers, A. Knorr, and T. Elsaesser, Ultrafast nonequilibrium carrier dynamics in a single graphene layer, Phys. Rev. B **83,** 153410 (2011).

[23] A. Betz, S. H. Jhang, E. Pallecchi, R. Ferreira, G. Fève, J.-M. Berroir, and B. Plaçais, Supercollision cooling in undoped graphene, Nat. Phys. **9,** 109 (2013).

[24] J. C. Song, M. Y. Reizer, and L. S. Levitov, Disorder-Assisted Electron-Phonon Scattering and Cooling Pathways in Graphene, Phys. Rev. Lett. **109,** 106602 (2012).

[25] D. Brida, A. Tomadin, C. Manzoni, Y. J. Kim, A. Lombardo, S. Milana, R. R. Nair, K. S. Novoselov, A. C. Ferrari, and G. Cerullo, Ultrafast collinear scattering and carrier multiplication in graphene, Nat. Commun. **4,** 1987 (2013).

[26] P. Borowik, J.-L. Thobel, and L. Adamowicz, Modified Monte Carlo method for study of electron transport in degenerate electron gas in the presence of electron–electron interactions, application to graphene, J. Comput. Phys. **341,** 397 (2017).

[27] X. Li, E. Barry, J. Zavada, M. B. Nardelli, and K. Kim, Influence of electron-electron scattering on transport characteristics in monolayer graphene, Appl. Phys. Lett. **97,** 082101 (2010).

[28] O. Bonno and J.-L. Thobel, Monte Carlo modeling of carrier-carrier scattering in semiconductors with non-parabolic bands, J. Appl. Phys. **104,** 053719 (2008).

[29] H. U. Chae, R. Ahsan, Q. Lin, D. Sarkar, F. Rezaeifar, S. B. Cronin, and R. Kapadia, High quantum efficiency hot electron electrochemistry, Nano Lett. **19,** 6227 (2019).

[30] See the Supplemental Material at http://link.aps.org/supplemental/10.1103/PhysRevApplied.13.024060 for detailed calculations.

[31] W. A. Harrison, Tunneling from an independent-particle point of view, Phys. Rev. **123,** 85 (1961).

[32] Y. S. Ang and L. Ang, in *2018 31st International Vacuum Nanoelectronics Conference (IVNC), IEEE* (2018), pp. 1–2.

[33] S. Meshkov, in *AIP Conference Proceedings, AIP* (1990), pp. 185–191.

[34] S. de Vega and F. J. García de Abajo, Plasmon generation through electron tunneling in graphene, ACS Photonics **4,** 2367 (2017).

[35] A. C. Neto, F. Guinea, N. M. Peres, K. S. Novoselov, and A. K. Geim, The electronic properties of graphene, Rev. Mod. Phys. **81,** 109 (2009).

[36] D. Sinha and J. U. Lee, Ideal graphene/silicon Schottky junction diodes, Nano Lett. **14,** 4660 (2014).

[37] F. H. Faisal, A theory of multiple photon absorption by graphene in intense laser fields, Ann. Phys. **525,** 171 (2013).

[38] F. H. Faisal, *Theory of Multiphoton Processes* (Springer US, 2013).

[39] J. K. Bae, I. Bazarov, P. Musumeci, S. Karkare, H. Padmore, and J. Maxson, Brightness of femtosecond nonequilibrium photoemission in metallic photocathodes at wavelengths near the photoemission threshold, J. Appl. Phys. **124,** 244903 (2018).

[40] J. Maxson, P. Musumeci, L. Cultrera, S. Karkare, and H. Padmore, Ultrafast laser pulse heating of metallic photocathodes and its contribution to intrinsic emittance, Nucl. Instrum. Methods Phys. Res. A **865,** 99 (2017).

[41] J. K. Bae, H. Padmore, I. Bazarov, S. Karkare, P. Musumeci, X. Shen, J. Maxson, and L. Cultrera, Multi-photon Photoemission and Ultrafast Electron Heating in Cu Photocathodes at Threshold, TUPML026 (2018).

[42] T. Saule, S. Heinrich, J. Schötz, N. Lilienfein, M. Högner, O. deVries, M. Plötner, J. Weitenberg, D. Esser, and J. Schulte, High-flux ultrafast extreme-ultraviolet photoemission spectroscopy at 18.4MHz pulse repetition rate, Nat. Commun. **10,** 458 (2019).

[43] X. Jiang, C. Berglund, A. E. Bell, and W. A. Mackie, OS3: Photoemission from gold thin films for application in multiphotocathode arrays for electron beam lithography, J. Vac. Sci. Technol. B Microelectron. Nanometer Struct. Process. Meas. Phenom. **16,** 3374 (1998).

[44] I. V. Bazarov, D. G. Ouzounov, B. M. Dunham, S. A. Belomestnykh, Y. Li, X. Liu, R. E. Meller, J. Sikora, C. K. Sinclair, and F. W. Wise, Efficient temporal shaping of electron distributions for high-brightness photoemission electron guns, Phys. Rev. Spec. Top.-Accel. Beams **11,** 040702 (2008).

[45] L. Cultrera, C. Gulliford, A. Bartnik, H. Lee, and I. Bazarov, Rb based alkali antimonide high quantum efficiency photocathodes for bright electron beam sources and photon detection applications, J. Appl. Phys. **121,** 055306 (2017).

[46] K. Torgasin, K. Morita, H. Zen, K. Masuda, M. Bakr, K. Nagasaki, T. Kii, and H. Ohgaki, Study on anomalous photoemission of LaB6 at high temperatures, Phys. Scr. **94,** 075701 (2019).

[47] T. Srinivasan-Rao, J. Fischer, and T. Tsang, Photoemission studies on metals using picosecond ultraviolet laser pulses, J. Appl. Phys. **69,** 3291 (1991).

[48] L. Blankemeier, F. Rezaeifar, A. Garg, and R. Kapadia, Integrated photonics for low transverse emittance, ultrafast negative electron affinity GaAs photoemitters, J. Appl. Phys. **126,** 033102 (2019).

[49] F. Rezaeifar and R. Kapadia, Efficient and ultrafast optical modulation of on-chip thermionic emission using resonant cavity coupled electron emitters, J. Vac. Sci. Technol. B **34,** 041228 (2016).

[50] F. Rezaeifar, Q. Lin, X. Chen, T. M. Mattox, A. Garg, A. Clough, N. Poudel, L. Blankemeier, D. Sarkar, S. B. Cronin, and R. Kapadia, Independent tuning of work function and field enhancement factor in hybrid lanthanum hexaboride-graphene-silicon field emitters, J. Vac. Sci. Technol. B **35,** 062202 (2017).